CrossMark

J. Fluid Mech. (2017), *vol.* 828, *pp.* 271–288. © Cambridge University Press 2017
doi:10.1017/jfm.2017.515

Morphological evolution of microscopic dewetting droplets with slip

Tak Shing Chan[1,†], Joshua D. McGraw[2], Thomas Salez[3,4], Ralf Seemann[1] and Martin Brinkmann[1]

[1]Experimental Physics, Saarland University, D-66041 Saarbrücken, Germany

[2]Département de Physique, Ecole Normale Supérieure/PSL Research University, CNRS, 24 rue Lhomond, 75005 Paris, France

[3]Laboratoire de Physico-Chimie Théorique, UMR CNRS Gulliver 7083, ESPCI Paris, PSL Research University, Paris, France

[4]Global Station for Soft Matter, Global Institution for Collaborative Research and Education, Hokkaido University, Sapporo, Japan

(Received 2 December 2016; revised 16 July 2017; accepted 25 July 2017; first published online 4 September 2017)

We investigate the dewetting of a droplet on a smooth horizontal solid surface for different slip lengths and equilibrium contact angles. Specifically, we solve for the axisymmetric Stokes flow using the boundary element method with (i) the Navier-slip boundary condition at the solid/liquid boundary and (ii) a time-independent equilibrium contact angle at the contact line. When decreasing the rescaled slip length $\tilde{b}$ with respect to the initial central height of the droplet, the typical non-sphericity of a droplet first increases, reaches a maximum at a characteristic rescaled slip length $\tilde{b}_m \approx O(0.1\text{–}1)$ and then decreases. Regarding different equilibrium contact angles, two universal rescalings are proposed to describe the behaviour of the non-sphericity for rescaled slip lengths larger or smaller than $\tilde{b}_m$. Around $\tilde{b}_m$, the early time evolution of the profiles at the rim can be described by similarity solutions. The results are explained in terms of the structure of the flow field governed by different dissipation channels: elongational flows for $\tilde{b} \gg \tilde{b}_m$, friction at the substrate for $\tilde{b} \approx \tilde{b}_m$ and shear flows for $\tilde{b} \ll \tilde{b}_m$. Following the changes between these dominant dissipation mechanisms, our study indicates a crossover to the quasistatic regime when $\tilde{b}$ is many orders of magnitude smaller than $\tilde{b}_m$.

Key words: capillary flows, contact lines, interfacial flows (free surface)

1. Introduction

A classical problem of dynamic wetting is the spreading of a droplet when it is placed in contact with a smooth and chemically homogeneous substrate (Chen 1988; Bonn *et al.* 2009). For complete wetting, with a vanishing equilibrium contact angle, the spreading process follows the well-known Tanner's law (Voinov 1976; Tanner 1979) stating that the contact line radius R grows in time t as a power law $R \sim t^{1/10}$.

† Email address for correspondence: tak.chan@physik.uni-saarland.de

https://doi.org/10.1017/jfm.2017.515 Published online by Cambridge University Press

This asymptotically valid relation is derived with the assumption that the droplet maintains a spherical-cap-shaped profile during spreading, except in the vicinity of the moving contact line, where the interface is deformed strongly due to viscous stresses. The general assumptions of a quasistatic macroscopic interface profile and a quasisteady viscous flow in the region close to the contact line have been central guidelines in studies of dynamic wetting problems (Bonn *et al.* 2009; Snoeijer & Andreotti 2013; Sui, Ding & Spelt 2014). Examples include industrial applications such as oil recovery (Sahimi 1993), immersion lithography (Winkels *et al.* 2011) and coating (Weinstein & Ruschak 2004), as well as natural phenomena (Bonn *et al.* 2009) such as liquid droplets sliding on the surface of a leaf. The basis of these assumptions lies in the wide separation of length scales between the extension of the interface and a microscopic length to relax the singularity of infinite viscous dissipation (Huh & Scriven 1971) at the contact line. As specifically discussed here, this microscopic length scale may be the slip length, defined as the ratio between the fluid velocity parallel to the substrate and the shear rate at the boundary. In cases where a no-slip condition is assumed for the solid/liquid boundary, other microscopic length scales in specific models have been proposed as reviewed in Bonn *et al.* (2009), Snoeijer & Andreotti (2013) and Sui *et al.* (2014).

In the context of hydrodynamics, slippage refers to the phenomenon that fluids may flow with non-zero velocity along a solid/liquid boundary. Although the microscopic origin of slippage depends on the material parameters of solid/liquid pair under consideration (Lauga, Brenner & Stone 2007), there have been extensive studies on the measurement of the slip length due to the development of new experimental techniques in recent years (Neto *et al.* 2005; Bocquet & Charlaix 2009; Guo *et al.* 2013). Interestingly, slip lengths as large as a few micrometres have been reported in some studies using polymer melts (Reiter & Sharma 2001; Leger 2003; Fetzer *et al.* 2005, 2007; Bäumchen, Fetzer & Jacobs 2009; Haefner *et al.* 2015). These findings raise fundamental questions on the description of the contact line motion and the evolution of the interface profile, particularly in micrometric (Cuenca & Bodiguel 2013; Setu *et al.* 2015) or nanometric (Falk *et al.* 2010) systems, for which the separation of length scales may not be fulfilled.

The opposite process of spreading (wetting), called dewetting, occurs when the driving forces tend to decrease the contact area between the liquid and the solid (de Gennes, Brochart-Wyart & Quéré 2003). Dewetting has been commonly studied in the geometry of liquid films (Redon, Brochard-Wyart & Rondelez 1991; Snoeijer & Eggers 2010; Rivetti *et al.* 2015). In these situations, due to the accumulation of mass in the contact line region, a bump of liquid is naturally formed in a rim. In the case of no slip or weak slip, namely the slip length is orders of magnitude smaller than the height of the bump; the bump maintains a static shape with a growing size (i.e. quasistatic), and the contact line moves at a constant speed (Redon *et al.* 1991; Snoeijer & Eggers 2010). Recently, the dewetting of flat droplets on a solid surface has been studied in detail (Edwards *et al.* 2016). In that study, the ratio between the slip length ($\approx$1 nm) and the central height of the droplets is approximately 10^{-5}. The dewetting process has been found to be similar to that of liquid films (Redon *et al.* 1991; Snoeijer & Eggers 2010), except the final state is a single droplet. In this weak-slip regime, the slip length effectively acts as a cutoff length for the contact line singularity, and only has a weak effect (logarithmic dependence) on the dynamics. A recent study on dewetting polymer microdroplets (McGraw *et al.* 2016), however, showed that the transient droplet shape evolution, in the regime where the slip length is comparable to or larger than the typical droplet size (i.e. $\tilde{b} \approx O(0.1\text{–}10)$), is much

https://doi.org/10.1017/jfm.2017.515 Published online by Cambridge University Press

richer than one expects under the assumptions of quasistatic profiles and dissipation localized near the contact line. The transient droplet profiles are indeed found to be non-spherical (i.e. non-quasistatic), and highly dependent on the precise value of the slip length. One characteristic feature of the dewetting process is the development of a transient ridge for relatively small slip lengths. The ridge was found to be more pronounced when the slip length is smaller, and avoided for larger slip lengths due to elongational flow inside the droplet. On the other hand, as discussed above, when the slip length is many orders of magnitude smaller than the droplet size, one expects to recover the typical quasistatic sequence of spherical-cap-shaped profiles.

In this article, we study the dewetting of a flat viscous droplet for a wide range of slip lengths and various equilibrium contact angles employing the boundary element method. We elucidate the transition between the quasistatic and non-quasistatic evolutions of a dewetting droplet. The non-sphericity of the droplet increases when the slip length is first decreased from the full-slip limit. Further decreasing the slip length, we observe a new feature with respect to previous works (McGraw *et al.* 2016): the non-sphericity reaches a maximum and then starts to decrease. This behaviour is demonstrated for different equilibrium contact angles. We give explanations for these results in terms of flow structures and the spreading of a localized ridge.

2. Formulation

As an initial condition, we consider a spherical-cap-shaped droplet sitting on a plane and smooth substrate with a contact angle θ_i, which is smaller than the equilibrium contact angle θ_e. In order to minimize the surface energy, the droplet starts to retract and approaches a spherical cap with the equilibrium contact angle. Because of the homogeneous and planar substrate, the shape of the droplet remains axisymmetric during its evolution. The droplet profile is described by the height, $h(r, t)$, of the liquid with respect to the substrate as a function of the radial distance from the central axis r and time t. We further assume the liquid inside the droplet to be a highly viscous and incompressible Newtonian liquid so that the flow obeys the Stokes equation,

$$\eta \nabla^2 \boldsymbol{u} - \boldsymbol{\nabla} p = 0, \tag{2.1}$$

and the continuity equation which reads

$$\boldsymbol{\nabla} \cdot \boldsymbol{u} = 0, \tag{2.2}$$

where $\boldsymbol{u}$ and p are the velocity field and the pressure field in the liquid, respectively, and η is the dynamic viscosity of the liquid.

To solve for the flow fields and the evolution of the interface profile, one needs to specify appropriate boundary conditions. First, the stress tensor $\boldsymbol{\sigma}$ in Cartesian coordinates is given as

$$\sigma_{ij} = -p\delta_{ij} + \eta \left(\frac{\partial u_i}{\partial x_j} + \frac{\partial u_j}{\partial x_i} \right), \tag{2.3}$$

and the stress $\boldsymbol{f}$ at the boundary reads

$$\boldsymbol{f} = \boldsymbol{\sigma} \cdot \hat{\boldsymbol{n}}. \tag{2.4}$$

Here $\hat{\boldsymbol{n}}$ is the unit vector normal to the boundary of the droplet pointing into the enclosed fluid.

https://doi.org/10.1017/jfm.2017.515 Published online by Cambridge University Press

Assuming the surrounding air flow is negligible, the tangential stress vanishes at the liquid/air boundary. The normal stress $f_n^{free} \equiv \boldsymbol{f}^{free} \cdot \hat{\boldsymbol{n}}$ at the free surface is balanced by the surface tension, leading to the Young–Laplace law:

$$f_n^{free} = 2\gamma\kappa, \tag{2.5}$$

where γ denotes the interfacial tension and κ the mean curvature of the free surface, which is defined as

$$\kappa = \frac{\dfrac{\partial^2 h}{\partial r^2}}{2\left(1+\left(\dfrac{\partial h}{\partial r}\right)^2\right)^{3/2}} + \frac{\dfrac{\partial h}{\partial r}}{2r\left(1+\left(\dfrac{\partial h}{\partial r}\right)^2\right)^{1/2}}. \tag{2.6}$$

Note that disjoining pressures are not considered in this model. The evolution of the interface profile is given by the kinematic condition along the free interface, that is

$$\frac{\partial h}{\partial t} = u_z - \frac{\partial h}{\partial r} u_r. \tag{2.7}$$

At the solid/liquid boundary, the velocity normal to the wall vanishes. Regarding the velocity component parallel to the wall $u_t^{wall}\hat{\boldsymbol{r}}$, we impose a Navier-slip condition which reads

$$u_t^{wall} = \frac{b}{\eta} f_t^{wall}, \tag{2.8}$$

where $\hat{\boldsymbol{r}}$ is the unit vector in the radial direction, $f_t^{wall} \equiv \boldsymbol{f}^{wall} \cdot \hat{\boldsymbol{r}}$ is the shear stress at the wall and the slip length, b, is assumed to be a constant. To complete the hydrodynamic problem, we impose the condition that the free surface touches the wall with a finite contact angle. This angle is assumed to be the same as the equilibrium contact angle θ_e, independent of the contact line velocity. Moreover, since the substrate surface is smooth and chemically homogeneous, θ_e is also independent of the contact line position.

2.1. *Boundary element method (BEM)*

The Stokes equation (2.1) and the continuity equation (2.2) can be formulated in the form of the boundary integral equations; a method which has been used extensively to study many interfacial flow problems (Pozrikidis 1992). In this approach the velocity $\boldsymbol{u}(\boldsymbol{s}_0)$ at any point $\boldsymbol{s}_0$ can be written in terms of integrals involving the stress $\boldsymbol{f}$ and the velocity on the boundary. For the axisymmetric Stokes flow problem we study in this article, the boundary integral equations (Pozrikidis 1992) read

$$u_\alpha(\boldsymbol{s}_0) = -\frac{A}{4\pi\eta}\int_c \bar{G}_{\alpha\beta}(\boldsymbol{s}_0, \boldsymbol{s}) f_\beta(\boldsymbol{s})\,\mathrm{d}l(\boldsymbol{s}) + \frac{A}{4\pi}\int_c \bar{T}_{\alpha\beta\zeta}(\boldsymbol{s}_0, \boldsymbol{s}) u_\beta(\boldsymbol{s}) n_\zeta(\boldsymbol{s})\,\mathrm{d}l(\boldsymbol{s}), \tag{2.9}$$

where the subscripts α, β and ζ represent either the radial (r) or the vertical (z) components in cylindrical coordinates, and c is the contour line (boundary) over which the integration takes place. The repeated Greek indices conform to the Einstein summation convention, that is they are summed over the radial and the vertical components. For the expression of the tensor components $\bar{G}_{\alpha\beta}$ and $\bar{T}_{\alpha\beta\zeta}$, we refer to § A.1. The value of A depends on the position $\boldsymbol{s}_0$:

$$A = \begin{cases} 1/2 & \text{for } \boldsymbol{s}_0 \text{ inside the liquid domain enclosed by the boundary,} \\ 1 & \text{for } \boldsymbol{s}_0 \text{ on the closed boundary.} \end{cases} \tag{2.10}$$

https://doi.org/10.1017/jfm.2017.515 Published online by Cambridge University Press

We note that $\bar{G}_{\alpha\beta}$ and $\bar{T}_{\alpha\beta\zeta}$ are singular at $\boldsymbol{s}=\boldsymbol{s}_0$; the integral over the singular point is thus computed analytically by expanding the tensor components in series about $\boldsymbol{s}=\boldsymbol{s}_0$ (Lee & Leal 1982; van Lengerich & Steen 2012).

The main advantage of the boundary element method is that the velocity field is explicitly written in terms of the velocities and the stresses on the boundary. No discretization of elements inside the droplet is required to solve for the flow fields. As given by the boundary conditions, not all the velocities and stresses at the boundary of the liquid domain are known. For example, the velocities at the free interface are unknowns, yet the unknown quantities can be found by solving (2.9) for the case that $\boldsymbol{s}_0$ lies on the boundary. For a numerical treatment of the problem, the contour is discretized into small linear elements. The velocity and the stress are taken to be constant within the same element. A system of linear equations is then obtained from (2.9), and the unknown quantities can be computed. Note that the normal stress for the numerical element of the liquid/air interface containing the contact line is computed with the boundary condition of the imposed equilibrium contact angle θ_e. Once the velocities at the free surface have been computed, one can determine the profile evolution using the kinematic condition (2.7).

Initially, the droplet has a spherical-cap shape with a contact angle θ_i. Due to the small molecular relaxation time scale at the contact line, the contact angle quickly reaches the equilibrium contact angle θ_e microscopically (McGraw *et al.* 2016). To approximate this initial microscopic contact angle in our numerical computations, we assume that at $t=0$, there is a kink in the interface profile at the contact line position. The line connecting the first numerical marker point and the contact line makes an angle θ_e with the substrate. Due to this kink, the magnitude of the approximated interfacial curvature near the contact line is larger than that on the rest of the interface, thus the Laplace pressure is unbalanced and the pressure gradient initiates a flow. Hence, the contact line starts to move towards the centre. The kink then quickly relaxes to a smooth shape due to surface tension. This type of initial profile is a natural choice as it smoothly connects the boundary condition at the contact line and the initial spherical-cap shape of the droplet. Note that our model is not able to describe the physics happening in the very vicinity of the contact line at earlier times. A different approach from hydrodynamics is required to solve that specific problem, such as molecular dynamics simulations.

We non-dimensionalize the problem as follows: all lengths are rescaled by the initial maximum height of the droplet h_0 and all the times by the viscous capillary time scale $h_0\eta/\gamma$. All these dimensionless variables are denoted with a tilde. We are thus left with three independent dimensionless parameters. In the following, we consider the initial contact angle θ_i, the equilibrium contact angle θ_e and the rescaled slip length $\tilde{b}\equiv b/h_0$ as the control parameters. For all our numerical computations, 300 marker points are used to describe the interface profile of the droplet. The vertical separation between two marker points is approximately 0.003. For smaller separations, the profile evolution becomes unstable. We then set the smallest rescaled slip length to $\tilde{b}=0.023$, which is about ten times the marker separation. Hence for all our computations, the rescaled slip length is varied in a range $\tilde{b}>0.023$. We also check the conservation of volume in our numerics. The difference between the initial and the final volumes of the droplets is less than 1 %. Further demonstrations of the numerical precision of our BEM, and a comparison to analytical results, are shown in § A.2.

3. Results and discussion

In this section, we present the results of our numerical computations. In § 3.1, we revisit the interfacial profile evolution as studied by McGraw *et al.* (2016).

https://doi.org/10.1017/jfm.2017.515 Published online by Cambridge University Press

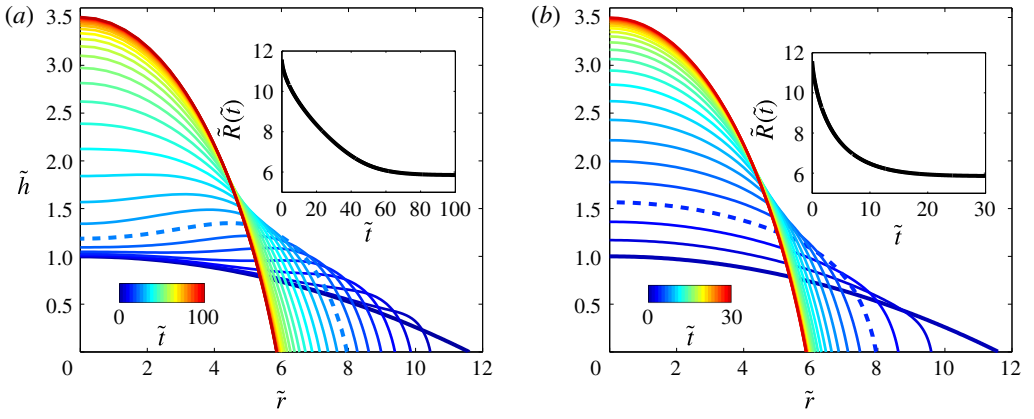

FIGURE 1. (Colour online) Evolution of the droplet profiles. The initial shape of the droplet is a flat spherical cap with contact angle $\theta_i = 10°$. The final equilibrium droplet has contact angle $\theta_e = 62°$. One of the profiles in each figure is plotted with a dashed line to emphasize the difference between the transient shapes. (*a*) $\tilde{b} = 0.46$. The time interval $\delta\tilde{t}$ between two neighbouring curves is 3.48. (*b*) $\tilde{b} = 23.2$ and $\delta\tilde{t} = 1.28$. Insets: the contact line position $\tilde{R}(\tilde{t})$ as a function of time $\tilde{t}$.

We characterize and quantify the deviation of the transient droplet profiles from a spherical cap. Then we investigate the temporal evolution of the non-sphericity and how the non-sphericity depends on the slip length and the equilibrium contact angle. The early time dynamics of the transient ridge is studied in § 3.2. In § 3.3 we rationalize the behaviour of the non-sphericity in terms of the flow structure and the spreading of the ridge.

3.1. *Interfacial profile evolution and non-sphericity of the profiles*

Here we briefly consider the droplet geometries studied in McGraw *et al.* (2016), namely an initial spherical cap with $\theta_i = 10°$ and an equilibrium contact angle $\theta_e = 62°$. As discussed in McGraw *et al.* (2016), the main feature of the profile evolution is the appearance, or absence, of a transient ridge, defined as the fluid region in between the contact line and the outermost inflection point of the droplet profile (i.e. $\partial^2\tilde{h}/\partial\tilde{r}^2|_{\tilde{r}=\tilde{r}_{inf}} = 0$). The ridge may develop to a global bump, characterized by a maximum in the height profile at $\tilde{r} \neq 0$. The properties of the global bump will be discussed in § 3.4. We first look at two different rescaled slip lengths, $\tilde{b} = 0.46$ and 23.2, which respectively demonstrate the formation or absence of a transient ridge. The evolution of the free interface profiles $\tilde{h}(\tilde{r}, \tilde{t})$ is shown in figure 1(*a*) for $\tilde{b} = 0.46$ and in figure 1(*b*) for $\tilde{b} = 23.2$. The main difference between the two cases is that, for $\tilde{b} = 0.46$, the profile around the centre does not change appreciably at early times. The fluid accumulates in a rim as the contact line moves towards the centre of the droplet and forms a transient ridge. In contrast, for $\tilde{b} = 23.2$, the height of the interface profile at the centre of the droplet increases at early times due to elongational flow (McGraw *et al.* 2016). No ridge is developed in this case.

The transient profiles of the droplets in both cases shown in figure 1 deviate significantly from the shape of a spherical cap. To quantify the non-sphericity of the droplet, we introduce an observable ΔV in the following way. For each time

https://doi.org/10.1017/jfm.2017.515 Published online by Cambridge University Press

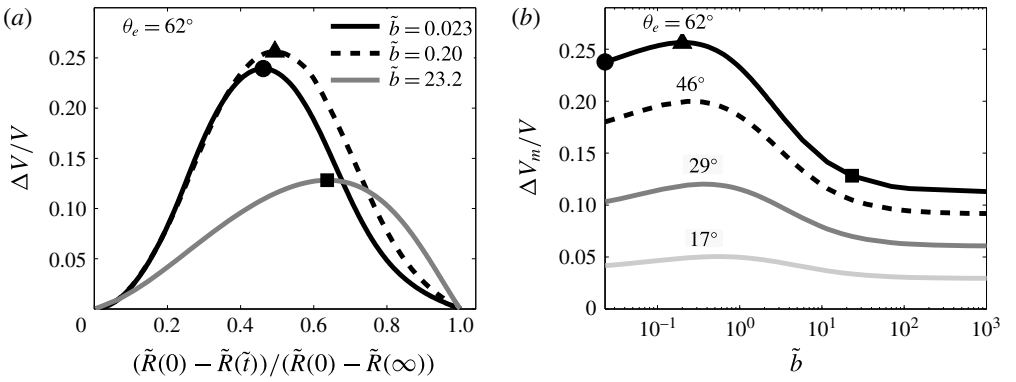

FIGURE 2. (*a*) The non-sphericity, $\Delta V/V$, versus the rescaled contact line displacement $(\tilde{R}(0) - \tilde{R}(\tilde{t}))/(\tilde{R}(0) - \tilde{R}(\infty))$ for $\theta_e = 62°$ and for three different slip lengths. The maxima are indicated by solid symbols. (*b*) The maximum of $\Delta V/V$ shown in (*a*), $\Delta V_m/V$, as a function of slip length $\tilde{b}$ for different equilibrium contact angles θ_e. For both (*a*) and (*b*), the initial contact angle is $\theta_i = 10°$.

$\tilde{t}$, we determine the spherical cap of profile $\tilde{z} = \tilde{S}(\tilde{r}, \tilde{t}; \tilde{\rho}, \tilde{S}_0)$ that best fits the profile of the droplet; $\tilde{S}$ is given implicitly by $\tilde{\rho}^2 = \tilde{r}^2 + (\tilde{S} - \tilde{S}_0)^2$, where $\tilde{S}_0$ is the vertical shift of the sphere centre while $\tilde{\rho}$ is its radius of curvature. We introduce ΔV as the total volume of the non-overlapped region between the droplet and the corresponding spherical cap. The spherical cap is selected under the condition that the total non-overlapped volume is minimized. More precisely, we define

$$\Delta V = \min_{\tilde{\rho}, \tilde{S}_0} \left(\int_0^\infty \mathrm{d}\tilde{r} 2\pi \tilde{r} |\tilde{h}(\tilde{r}, \tilde{t}) - \tilde{S}(\tilde{r}, \tilde{t}; \tilde{\rho}, \tilde{S}_0)| \right), \tag{3.1}$$

under the constraint of identical total volumes:

$$V = \int_0^\infty \mathrm{d}\tilde{r} 2\pi \tilde{r} \tilde{h}(\tilde{r}, \tilde{t}) = \int_0^\infty \mathrm{d}\tilde{r} 2\pi \tilde{r} \tilde{S}(\tilde{r}, \tilde{t}; \tilde{\rho}, \tilde{S}_0). \tag{3.2}$$

Note that

$$\left.\begin{array}{ll} \tilde{h}(\tilde{r}, \tilde{t}) = 0 & \text{for } \tilde{r} > \tilde{R}(\tilde{t}), \\ \tilde{S}(\tilde{r}, \tilde{t}; \tilde{\rho}, \tilde{S}_0) = 0 & \text{for } \tilde{r} > \tilde{R}_{cap}(\tilde{t}; \tilde{\rho}, \tilde{S}_0), \end{array}\right\} \tag{3.3}$$

where $\tilde{R}(\tilde{t})$ and $\tilde{R}_{cap}(\tilde{t}; \tilde{\rho}, \tilde{S}_0)$ are the contact line radius of the droplet and the spherical cap respectively.

In figure 2(*a*), ΔV rescaled by the volume of the droplet is plotted as a function of the contact line displacement $\tilde{R}(0) - \tilde{R}(\tilde{t})$ normalized by the total displacement $\tilde{R}(0) - \tilde{R}(\infty)$ for $\tilde{b} = 0.023$, 0.20 and 23.2. For all three cases, $\Delta V/V$ is zero at $\tilde{t} = 0$ and at equilibrium because of the spherical-cap shape of the droplets. During the evolution, the non-sphericity attains a maximum. This maximal non-sphericity, $\Delta V_m/V$, occurs at smaller contact line displacements for smaller slip lengths.

A full investigation of $\Delta V_m/V$ as a function of $\tilde{b}$ is shown in figure 2(*b*) for various θ_e. We observe that this maximal non-sphericity of the droplet evolution is non-monotonic with $\tilde{b}$ for all θ_e investigated. We note furthermore the presence

https://doi.org/10.1017/jfm.2017.515 Published online by Cambridge University Press

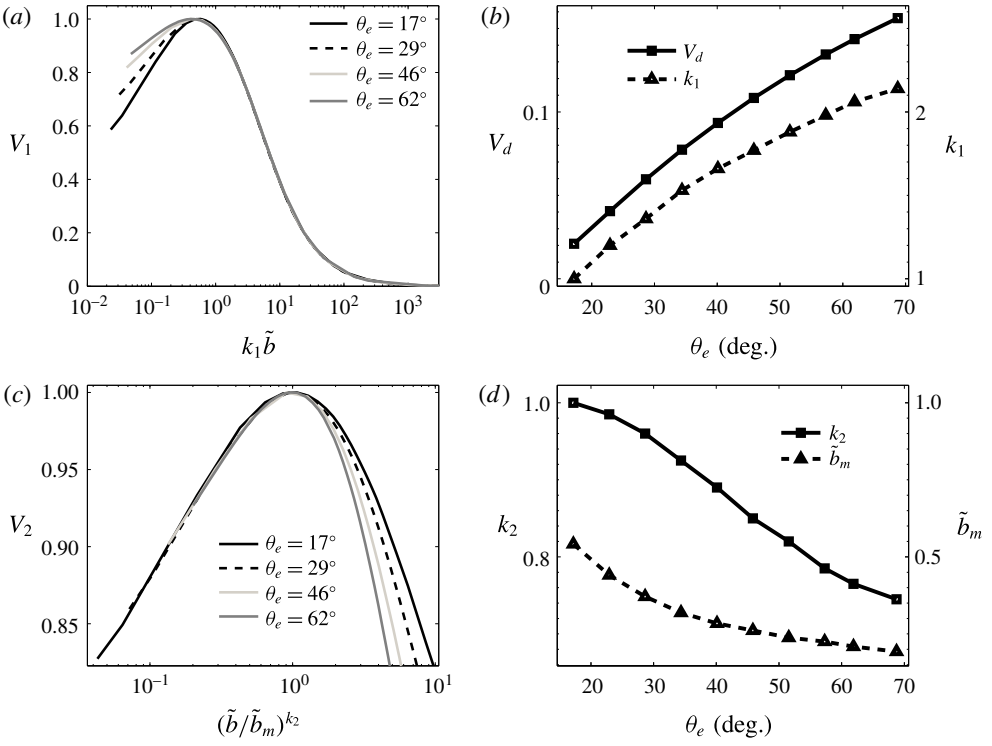

FIGURE 3. After two different rescalings, the data in figure 2(*b*) collapse onto a single function for two different regions, namely $\tilde{b} > \tilde{b}_m$ as shown in (*a*) and for $0.023 < \tilde{b} < \tilde{b}_m$ as shown in (*c*). (*a*) V_1, defined as $(\Delta V_m/V - \Delta V_m(\infty)/V)/V_d$, versus $k_1\tilde{b}$. (*b*) The dependence of V_d and k_1 on the equilibrium contact angle θ_e. (*c*) V_2, defined as $\Delta V_m/V$ rescaled by $\Delta V_m(\tilde{b}_m)/V$, versus $(\tilde{b}/\tilde{b}_m)^{k_2}$. (*d*) $\tilde{b}_m$ and k_2 as a function of θ_e.

of a well-defined maximum at a slip length that we denote by $\tilde{b}_m(\theta_e)$. For $\tilde{b} > \tilde{b}_m$, $\Delta V_m/V$ decreases with $\tilde{b}$ and asymptotically saturates to a finite $\Delta V_m(\infty)/V$. For $\tilde{b} < \tilde{b}_m$, $\Delta V_m/V$ decreases with decreasing $\tilde{b}$. As expected, the non-sphericity becomes smaller as the equilibrium contact angle θ_e approaches the initial contact angle θ_i.

The similar features of $\Delta V_m/V$ as a function of $\tilde{b}$ for different equilibrium contact angles θ_e suggest possible collapse of the curves after certain rescalings. First, we shift $\Delta V_m/V$ by $\Delta V_m(\infty)/V$ such that all the curves have the same reference level in the full-slip limit. Then we rescale the shifted $\Delta V_m/V$ by $V_d \equiv \Delta V_m(\tilde{b}_m)/V - \Delta V_m(\infty)/V$. We hence introduce a rescaled quantity $V_1(\tilde{b})$ as the following:

$$V_1(\tilde{b}) \equiv \frac{\Delta V_m(\tilde{b}) - \Delta V_m(\infty)}{\Delta V_m(\tilde{b}_m) - \Delta V_m(\infty)}. \tag{3.4}$$

The maximum of V_1 is unity for any equilibrium contact angles. When plotting V_1 versus $\tilde{b}$ multiplied by a scaling factor $k_1(\theta_e)$ in figure 3(*a*), we observe that the curves for different θ_e collapse into a single function for $\tilde{b} > \tilde{b}_m$. The dependence of V_d and k_1 on θ_e is shown in figure 3(*b*). Note that k_1 is not unique. The effect of k_1 is shifting

https://doi.org/10.1017/jfm.2017.515 Published online by Cambridge University Press

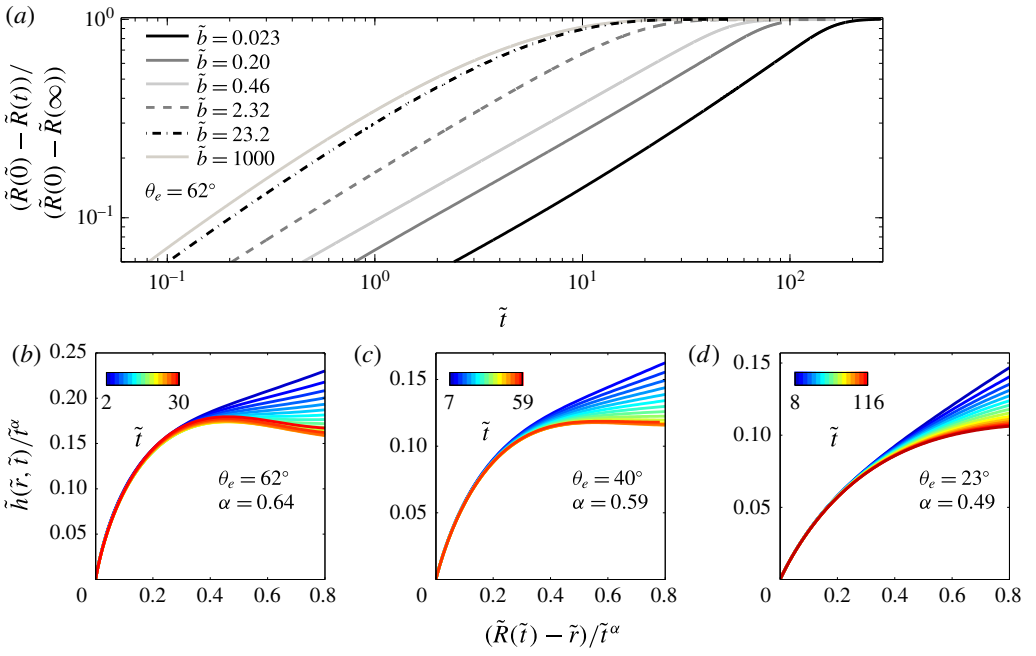

FIGURE 4. (Colour online) (*a*) Rescaled contact line displacement $(\tilde{R}_0 - \tilde{R}(\tilde{t}))/(\tilde{R}_0 - \tilde{R}_\infty)$ as a function of $\tilde{t}$ in log–log scale for different $\tilde{b}$ and fixed $\theta_e = 62°$. The early time data for intermediate slip lengths around $\tilde{b}_m$ can be described by a power law. A single power law becomes less pronounced for large and small slip lengths away from $\tilde{b}_m$. (*b–d*) Rescaled profiles for $\theta_e = 62°$ in (*b*), $\theta_e = 40°$ in (*c*) and $\theta_e = 23°$ in (*d*); $\tilde{b} = 0.46$ in all cases.

the curve horizontally. Multiplying k_1 by an arbitrary factor will still collapse all the curves. Here we take $k_1 = 1$ for $\theta_e = 17°$, which is the smallest equilibrium contact angle considered here.

For $0.023 < \tilde{b} < \tilde{b}_m$, a different rescaling is required to reach a collapse of the curves. In figure 3(*c*), V_2, defined as $\Delta V_m/V$ rescaled by $\Delta V_m(\tilde{b}_m)/V$, is plotted as a function of $(\tilde{b}/\tilde{b}_m)^{k_2}$; a single curve is thus obtained for $0.023 < \tilde{b} < \tilde{b}_m$. This rescaling suggests a relation of the form $V_2/k_2 \sim \log(\tilde{b}/\tilde{b}_m)$. Such a logarithmic relation is reminiscent of the weak-slip models for non-equilibrium droplets (de Gennes 1985; Cox 1986), in which the contact line dynamics and the interface profile also depend on the slip length logarithmically. The dependence of $\tilde{b}_m$ and k_2 on θ_e is shown in figure 3(*d*). The different rescalings for $\tilde{b} < \tilde{b}_m$ and $\tilde{b} > \tilde{b}_m$ indicate the existence of different regimes of the droplet retraction dynamics. The details will be discussed in the following sections.

3.2. *The transient ridge and early time dynamics*

As the initial driving force is at the contact line, it is important to examine the growth of the rim once the contact line has started to move. We first look at the motion of the contact line. To resolve the contact line motion for early times, we investigate the rescaled contact line displacement $\mathcal{R}(\tilde{t}) \equiv (\tilde{R}(0) - \tilde{R}(\tilde{t}))/(\tilde{R}(0) - \tilde{R}(\infty))$. For given $\theta_i = 10°$ and $\theta_e = 62°$, $\mathcal{R}(\tilde{t})$ as a function of time is plotted in figure 4(*a*) in log–log

https://doi.org/10.1017/jfm.2017.515 Published online by Cambridge University Press

scale for different $\tilde{b}$. For large $\tilde{b}$, the slope of the curves decreases with time. A power law is observed for intermediate slip lengths in the vicinity of $\tilde{b}_m$ corresponding to the maximal non-sphericity, ΔV_m. We recall that $\tilde{b}_m = 0.21$ for $\theta_e = 62°$. For example, for $\tilde{b} = 0.46$ and $0.12 < \tilde{t} < 30$, the relation, i.e. $\mathcal{R} \sim \tilde{t}^{\beta}$, describes the data with $\beta = 0.59$. The power-law relation becomes less pronounced when decreasing $\tilde{b}$ for $\tilde{b} < \tilde{b}_m$. For $\tilde{b} = 0.023$, the curve is seen to bend upward with time. Similar features are also observed for other equilibrium contact angles. The exponent β is found to be 0.57 for $\theta_e = 40°$ and 0.54 for $\theta_e = 23°$, when $\tilde{b} = 0.46$.

Given these power-law relations for slip lengths around $\tilde{b}_m$, it is instructive to investigate whether the interface profiles near the contact line can be described by a similarity solution. Assuming a similarity solution of the form $\tilde{h} = \tilde{t}^{\alpha} f((\tilde{R}(\tilde{t}) - \tilde{r})/\tilde{t}^{\alpha})$, we found that the rescaled profiles in the rim region collapse best for values of $\alpha = 0.64$ for $\theta_e = 62°$, 0.59 for $\theta_e = 40°$ and 0.49 for $\theta_e = 23°$. The corresponding rescaled profiles are shown in figure 4(*b–d*). Note that these exponents are slightly different from the exponent β for the contact line. The exponent 0.49 for the case of $\theta_e = 23°$, in which the interfacial slope is small, is close to the $\alpha = 1/2$ scaling predicted from the lubrication calculation for intermediate slip, namely when the dissipation is dominated by the friction at the substrate (McGraw *et al.* 2016).

3.3. *Physical explanation for the behaviour of the non-sphericity: flow structures and the spreading of the ridge*

In this section, we rationalize the non-monotonic behaviour of the non-sphericity in terms of the flow structure and the spreading of the ridge.

We compute the velocity field inside the droplet using the boundary integral equation (2.9) with $A = 1/2$. The flow fields inside the droplet when the contact line position $\tilde{R} = 10.82$ are shown in figure 5 for three different rescaled slip lengths $\tilde{b} = 0.023$, 0.21 and 23.2, and with the same equilibrium contact angle $\theta_e = 62°$. For $\tilde{b} \gg \tilde{b}_m$, low friction at the substrate promotes an elongational flow which affects the whole droplet in a very short time, see figure 5 for $\tilde{b} = 23.2$. Therefore, the central height of the droplet increases even at early times due to the upward flow in the centre. This prevents mass accumulation at the edge of the droplet. When decreasing $\tilde{b}$, the elongational flow becomes less dominant. The flow is concentrated in the rim, see figure 5 for $\tilde{b} = 0.023$ and 0.21. Mass is thus accumulated in the rim while the contact line is moving towards the droplet centre. As a consequence, a pronounced transient ridge is observed and the non-sphericity, $\Delta V_m/V$, becomes larger when decreasing $\tilde{b}$ for $\tilde{b} > \tilde{b}_m$.

For $\tilde{b}$ close to $\tilde{b}_m$, the ridge profiles in the early times can be described by similarity solutions as shown in § 3.2. For small equilibrium contact angles, the similarity solutions can be obtained from the intermediate-slip lubrication model in which the dissipation by the friction at the substrate becomes dominant (McGraw *et al.* 2016).

When further decreasing $\tilde{b}$ from $\tilde{b}_m$, the non-sphericity becomes less pronounced. For those small $\tilde{b}$ cases, the flow is more confined to the contact line region and presents a vertical parabolic profile associated with strong shear dissipation, see figure 5 for $\tilde{b} = 0.023$. In addition, similarity solutions cannot describe the early ridge profiles anymore. The question of how much mass is accumulated at the ridge depends on the contact line speed and how fast the mass is redistributed to the central

https://doi.org/10.1017/jfm.2017.515 Published online by Cambridge University Press

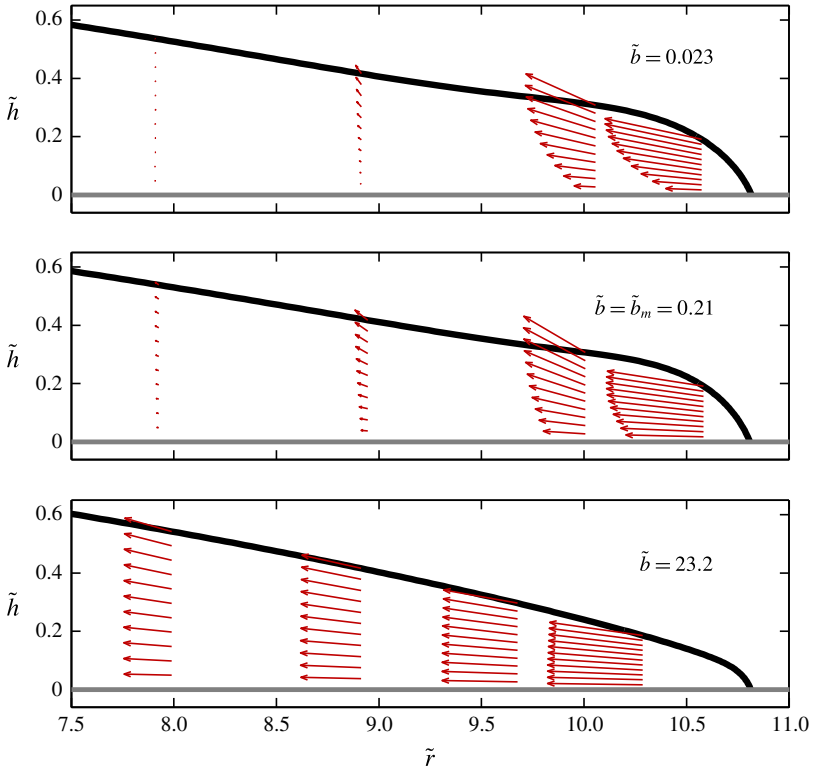

FIGURE 5. (Colour online) The flow fields for three different rescaled slip lengths $\tilde{b} = 0.023$, 0.21 and 23.2. The initial contact angle is $\theta_i = 10^\circ$ and the equilibrium contact angle is $\theta_e = 62^\circ$. The contact line position is $\tilde{R} = 10.82$.

part of the droplet by shear flow. This type of mass redistribution can be observed from the spreading of the ridge. One can imagine a situation when a contact line is pinned from a certain moment, the accumulated mass then has enough time to redistribute to the central part of the droplet and the development of a pronounced global ridge is avoided. Along this line of reasoning, we can understand the decrease of $\Delta V_m/V$ with decreasing $\tilde{b}$. The characteristic speed of the contact line decreases logarithmically with decreasing $\tilde{b}$ for small $\tilde{b}$ (McGraw *et al.* 2016), which means that the disturbance at the contact line will have more time to spread for smaller $\tilde{b}$. This result is demonstrated in figure 6(*a*,*b*) for the case of $\theta_e = 62^\circ$. In figure 6(*a*), several interface profiles are shown at the same contact line position for $\tilde{b} = 0.023$ and 0.14. For both cases, the slip lengths are smaller than $\tilde{b}_m$, so the shear dissipation dominates over the elongational one. One clearly sees that the ridge spreads wider for the smaller slip length, namely $\tilde{b} = 0.023$.

From the profiles of figure 6(*a*), we observe an outermost inflection point where $\mathrm{d}^2\tilde{h}/\mathrm{d}\tilde{r}^2 = 0$. The position of the inflection point $\tilde{r}_{inf}(\tilde{t})$ is used to characterize the extent of the ridge. The displacement of this inflection point $(\tilde{R}(0) - \tilde{r}_{inf}(\tilde{t}))$ normalized by $(\tilde{R}(0) - \tilde{R}(\infty))$ is plotted as a function of the rescaled contact line displacement in figure 6(*b*). It is found that first, the inflection point moves faster than the contact line for both cases, and second, for the same contact line position, the inflection point

https://doi.org/10.1017/jfm.2017.515 Published online by Cambridge University Press

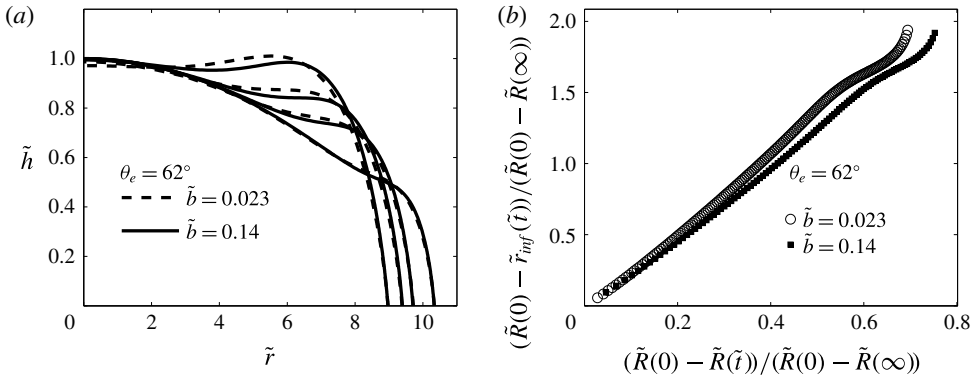

FIGURE 6. (*a*) Droplet profiles for $\tilde{b} = 0.023$ and 0.14. The profiles are compared when they have the same contact line position. (*b*) The rescaled displacement of the inflection point $(\tilde{R}(0) - \tilde{r}_{inf}(\tilde{t}))/(\tilde{R}(0) - \tilde{R}(\infty))$ versus the rescaled contact line displacement $(\tilde{R}(0) - \tilde{R}(\tilde{t}))/(\tilde{R}(0) - \tilde{R}(\infty))$.

displaces more for $\tilde{b} = 0.023$ compared to $\tilde{b} = 0.14$. This result shows again that mass is redistributed over a wider extent for the smaller slip length, $\tilde{b} = 0.023$. Hence the non-sphericity decreases with decreasing $\tilde{b}$. Although we are numerically limited to the smallest $\tilde{b} = 0.023$, from the trends shown in figure 2(*b*), we expect that $\Delta V_m/V$ diminishes in the limit of vanishing $\tilde{b}$. Our study thus indicates a crossover from a non-quasistatic regime to a quasistatic regime when $\tilde{b}$ is small.

3.4. *Characteristic of the global bump*

In this section we discuss the properties of the global bump, which reflects a global feature of the droplet profile. Understanding of this feature might be useful for droplet manipulations in micro- and nanofluidics. One can characterize the size of the global bump by measuring the difference between the maximum height of the profile and the central height of the droplet, which we refer to as the global-bump height. Like the non-sphericity $\Delta V_m/V$, the global-bump height attains a maximum value, denoted as h_b, throughout the profile evolution. A typical behaviour of h_b as a function of slip length $\tilde{b}$ is shown in figure 7(*a*) for $\theta = 62°$. The behaviours of $\Delta V_m/V$ and h_b are similar. The maximum bump height h_b is a non-monotonic function of the slip length and the maximum of h_b occurs at almost the same $\tilde{b}$ as for $\Delta V_m/V$. This indicates that the behaviour of both quantities have the same physical origin, namely the change of the flow structure when varying the slip length as discussed in § 3.3. For $\tilde{b}$ larger than the point of the maximum, we define the slip length at which h_b goes to zero as $\tilde{b} \equiv \tilde{b}^*$, which equals to 2.81 for the case of $\theta_e = 62°$. No transient global bump is observed for $\tilde{b} > \tilde{b}^*$.

Accessing more values of the equilibrium contact angle, we find an additional transition when $\tilde{b}$ is further decreased from $\tilde{b}^*$. For example, for $\theta_e = 34.5°$, $\tilde{b}^* = 0.79$, we observe a transition from 'with global bump' to 'without global bump' at a certain $\tilde{b}$, which is denoted as $\tilde{b}_L^*$ here, and equals 0.050 in this case. This result means a transient global bump exists only when $\tilde{b}_L^* < \tilde{b} < \tilde{b}^*$. This interesting behaviour can be observed clearly in figure 7(*b*) where the bump height h_b is plotted as a function of $\tilde{b}$.

https://doi.org/10.1017/jfm.2017.515 Published online by Cambridge University Press

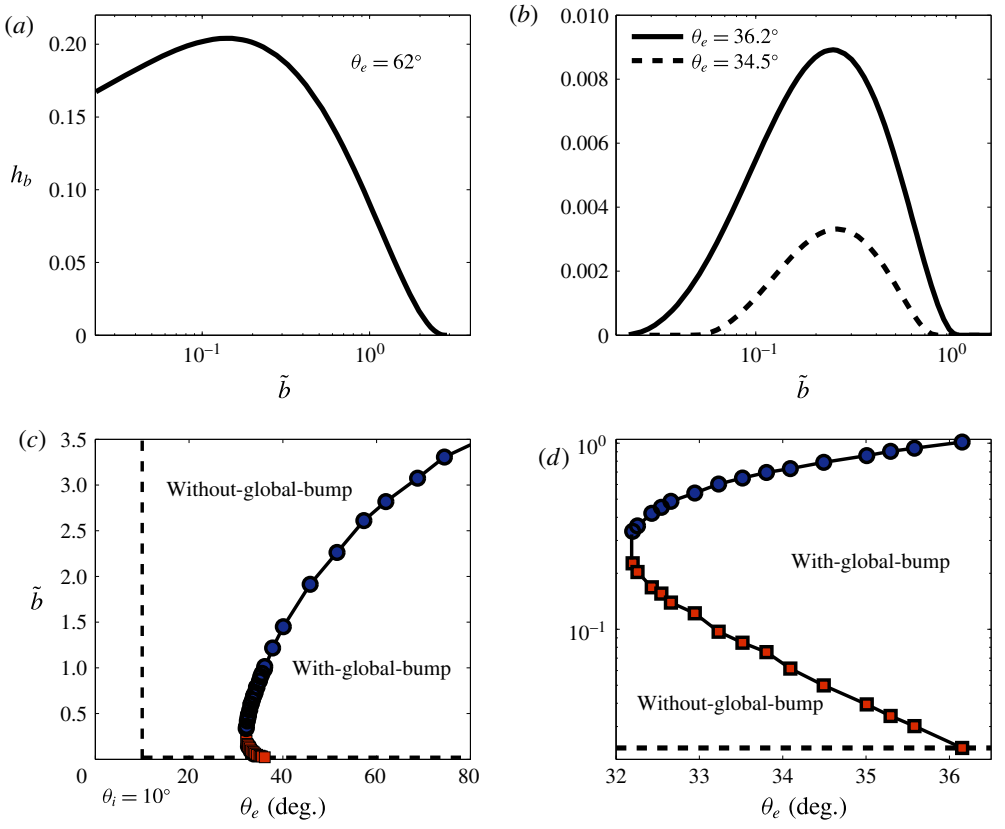

FIGURE 7. (Colour online) The global-bump height h_b versus $\tilde{b}$ for $\theta_i = 10°$. The equilibrium contact angle is $\theta_e = 62°$ in (*a*), $\theta_e = 34.5°$ or $36.2°$ in (*b*). (*c*) Phase diagram showing the with-global-bump region and the without-global-bump region. The vertical dashed line indicates the initial contact angle $\theta_i = 10°$. The horizontal dashed line indicates the smallest $\tilde{b}$ we have computed for, which is 0.023. Circles are b^* as a function of θ_e. Squares are $\tilde{b}_L^*$ as a function of θ_e. (*d*) Zoom on the region where $\tilde{b}_L^*$ is computed. Note that $\tilde{b}$ (*y*-axis) is in log scale.

To summarize the results, a phase diagram is plotted in figure 7(*c*,*d*) that indicates whether a global transient bump can be observed or not, for the specific case of $\theta_i = 10°$. When θ_e is close to θ_i, namely $\theta_e < 32.1°$, no global bump appears for any value of $\tilde{b}$. In these cases, a ridge is observed at the early stage for small slip lengths. However, a global bump (with a profile maximum not at $\tilde{r} = 0$) does not form because the initial and the final droplet shapes are too similar. In figure 7(*d*), one can observe the 'with-global-bump' region starts from $\theta_e = 32.1°$. Although the second transition is not observed for $\theta_e > 36.2°$ due to numerical limitations, we expect the bump to diminish in magnitude also for very small slip lengths in this case; the decrease of h_b in figure 7(*a*) for small $\tilde{b}$ supports this argument. Nevertheless, the slip length below which the global bump disappears is expected to be extremely small if the difference between the initial contact angle and the equilibrium contact angle is large. A recent study has demonstrated that a pronounced global bump exists in the dewetting of very flat droplets ($h_0/R(0) \approx 0.02$–0.1) even though the slip length is very small

https://doi.org/10.1017/jfm.2017.515 Published online by Cambridge University Press

($\tilde{b} \approx 10^{-5}$) (Edwards *et al.* 2016). In such cases, the transient global bump itself can be treated as quasistatic, as is the case in dewetting rims of thin liquid films (Redon *et al.* 1991; Snoeijer & Eggers 2010; Rivetti *et al.* 2015).

4. Conclusion

In this article, we study numerically the dewetting of a droplet, with an initial contact angle smaller than the equilibrium contact angle, using the boundary element method for axisymmetric Stokes flow. We impose the Navier-slip boundary condition at the solid/liquid boundary, and a time-independent equilibrium contact angle at the contact line position. The profile evolution is computed for a wide range of slip lengths ($2.3 \times 10^{-2} < \tilde{b} < 10^4$) and various equilibrium contact angles. For all our computations, the transient droplet profiles are found to deviate significantly from a spherical cap. We find that when decreasing the slip length, the typical non-sphericity first increases, reaches a maximum at a characteristic slip length $\tilde{b}_m$, and then decreases. This non-monotonic behaviour is found for all of the equilibrium contact angles investigated in this study, from $17^\circ \leqslant \theta_e \leqslant 69^\circ$.

The dependence of the non-sphericity on the slip length for different equilibrium contact angles can be described by two universal relations, one for $\tilde{b} > \tilde{b}_m$ and the other one for $0.023 < \tilde{b} < \tilde{b}_m$. This result indicates the existence of different flow structures depending on the value of $\tilde{b}$. For $\tilde{b} \gg \tilde{b}_m$, the flow is dominated by elongational flow. For $\tilde{b} \lesssim \tilde{b}_m$, the elongational flow becomes less important and the flow is confined in the rim at the beginning of the dewetting. Around $\tilde{b}_m$, the dissipation is dominated by the friction at the substrate as shown by the similarity solutions for the rim profile evolution at early times. When $\tilde{b} < \tilde{b}_m$, shear flow becomes more important. We rationalize the decrease of the non-sphericity with decreasing $\tilde{b}$ in terms of the spreading of the ridge and the contact line velocity. For smaller slip lengths, the accumulated mass due the movement of the contact line is redistributed to a wider extent, thus the droplet profile is closer to a spherical cap.

Although our numerical computations are limited to the smallest $\tilde{b} = 0.023$ we can access, the trend of the non-sphericity for $\tilde{b} < \tilde{b}_m$ implies that the transient droplet profile will be close to a spherical-cap shape when $\tilde{b}$ is very small, consistent with the expectation from the quasistatic approach. However, for a large difference between the initial and the equilibrium contact angles, the slip length below which the global bump disappears can be extremely small. In that case, the evolution of the global bump itself can be treated as quasistatic for small slip lengths. Our study thus brings a first prediction on the connection between the quasistatic and non-quasistatic regimes of droplet dewetting.

Acknowledgements

The authors thank S. Maurer, M. Benzaquen, E. Raphaël and K. Jacobs for a previous joint study on the topic. The authors also thank the Alexander von Humboldt Foundation and NSERC of Canada for financial support. The authors also acknowledge financial support from the Global Station for Soft Matter – a project of Global Institution for Collaborative Research and Education at Hokkaido University. J.D.M. was supported by LabEX ENS-ICFP: ANR-10-LABX-0010/ANR-10-IDEX-0001-02 PSL.

https://doi.org/10.1017/jfm.2017.515 Published online by Cambridge University Press

Appendix A

A.1. *Expressions of* $\bar{G}_{\alpha\beta}$ *and* $\bar{T}_{\alpha\beta\zeta}$

For the axisymmetric Stokes flow problem we study in this article, the boundary integral equation is quoted in (2.9). Here, we provide the standard expressions of the tensors $\bar{G}_{\alpha\beta}$ and $\bar{T}_{\alpha\beta\zeta}$. Note that different symbols are used for these tensors in the book of Pozrikidis (1992). First, we introduce a function I_{mn}, which is defined as

$$I_{mn} \equiv \frac{4k^m}{(4rr_0)^{m/2}} \int_0^{\pi/2} \frac{(2\cos^2 w - 1)^n}{(1 - k^2 \cos^2 w)^{m/2}} \, \mathrm{d}w. \tag{A 1}$$

k is given as

$$k \equiv \left(\frac{4rr_0}{z_d^2 + (r + r_0)^2} \right)^{1/2}, \tag{A 2}$$

and $z_d \equiv z - z_0$. Here (r, z) and (r_0, z_0) are the coordinates of $\boldsymbol{s}$ and $\boldsymbol{s}_0$ respectively.

For $\bar{G}_{\alpha\beta}$,

$$\bar{G}_{zz} = r(I_{10} + z_d^2 I_{30}), \tag{A 3}$$

$$\bar{G}_{zr} = rz_d(sI_{30} - r_0 I_{31}), \tag{A 4}$$

$$\bar{G}_{rz} = rz_d(rI_{31} - r_0 I_{30}), \tag{A 5}$$

$$\bar{G}_{rr} = r[I_{11} + (r^2 + r_0^2)I_{31} - rr_0(I_{30} + I_{32})]. \tag{A 6}$$

For $\bar{T}_{\alpha\beta\zeta}$,

$$\bar{T}_{zzz} = -6rz_d^3 I_{50}, \tag{A 7}$$

$$\bar{T}_{zzr} = \bar{T}_{zrz} = -6rz_d^2(rI_{50} - r_0 I_{51}), \tag{A 8}$$

$$\bar{T}_{zrr} = -6rz_d(r_0^2 I_{52} + r^2 I_{50} - 2rr_0 I_{51}), \tag{A 9}$$

$$\bar{T}_{rzz} = -6rz_d^2(rI_{51} - r_0 I_{50}), \tag{A 10}$$

$$\bar{T}_{rzr} = \bar{T}_{rrz} = -6rz_d[(r^2 + r_0^2)I_{51} - rr_0(I_{50} + I_{52})], \tag{A 11}$$

$$\bar{T}_{rrr} = -6r[r^3 I_{51} - r^2 r_0(I_{50} + 2I_{52}) + rr_0^2(I_{53} + 2I_{51}) - r_0^3 I_{52}]. \tag{A 12}$$

The tensors $\bar{G}_{\alpha\beta}$ and $\bar{T}_{\alpha\beta\zeta}$ have singular points at $\boldsymbol{s} = \boldsymbol{s}_0$ and $\boldsymbol{s} = 0$. Around these points, the boundary integral equation (2.9) is performed analytically by expanding $\bar{G}_{\alpha\beta}$ and $\bar{T}_{\alpha\beta\zeta}$ in series (van Lengerich & Steen 2012).

A.2. *Validation of the numerical method*

A.2.1. *Number of marker points*

The number of marker points M for the liquid/air interface used in the computations presented in this paper is $M = 300$. The convergence has been checked, see figure 8.

https://doi.org/10.1017/jfm.2017.515 Published online by Cambridge University Press

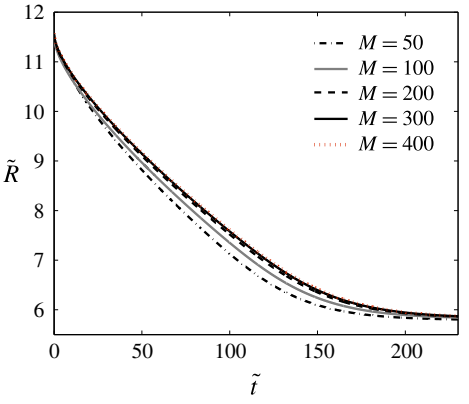

FIGURE 8. (Colour online) The contact line position $\tilde{R}$ as a function of time $\tilde{t}$ for $\theta_e = 62^\circ$ and $\tilde{b} = 0.023$.

The maximum difference between the curves for $M = 300$ and for $M = 400$ is 0.4 %, we thus conclude that $M = 300$ is sufficient to describe accurately the droplet evolution.

A.2.2. *Relaxation of a free droplet*

To validate our BEM, we consider the relaxation of a viscous ellipsoidal droplet of viscosity η surrounded by a inviscid fluid. The droplet is axisymmetric and the profile is described by $h(r, t)$. For small deformations, the profile maintains a shape of ellipse with the major axis denoted by $a(t)$ and the minor axis denoted by $b(t)$, namely

$$\frac{r^2}{a(t)^2} + \frac{h(r,t)^2}{b(t)^2} = 1, \tag{A 13}$$

for $0 \leqslant r \leqslant a(t)$. We define $D(t) \equiv (a(t) - b(t))/(a(t) + b(t))$. Applying Stokes equations, it has been proved analytically that $D(t)$ rescaled by the initial value $D_0 = D(t = 0)$ follows asymptotically the relation (Taylor 1934; Guido & Villone 1999)

$$\frac{D(t)}{D_0} = \exp(-40t/38). \tag{A 14}$$

Here t is the time rescaled by $R_0\eta/\gamma$, where R_0 is the radius of the droplet (of spherical shape) at $t \to \infty$.

To validate our BEM, we compare our computation with the above analytical formula (A 14). For our computation, we take the rescaled slip length $\tilde{b} = 10\,000$ and the equilibrium contact angle $\theta_e = 90^\circ$. As an initial condition, we consider $a(t = 0) = 1.1$ and $b(t = 0) = 1$. Figures 9(*a*) and 9(*b*) show the droplet profiles and the time series of $a(t)$ and $b(t)$ respectively. In figure 9(*c*), the variable $D(t)/D_0$ computed by BEM is shown to agree well with the analytical result of (A 14) with no free fitting parameter.

https://doi.org/10.1017/jfm.2017.515 Published online by Cambridge University Press

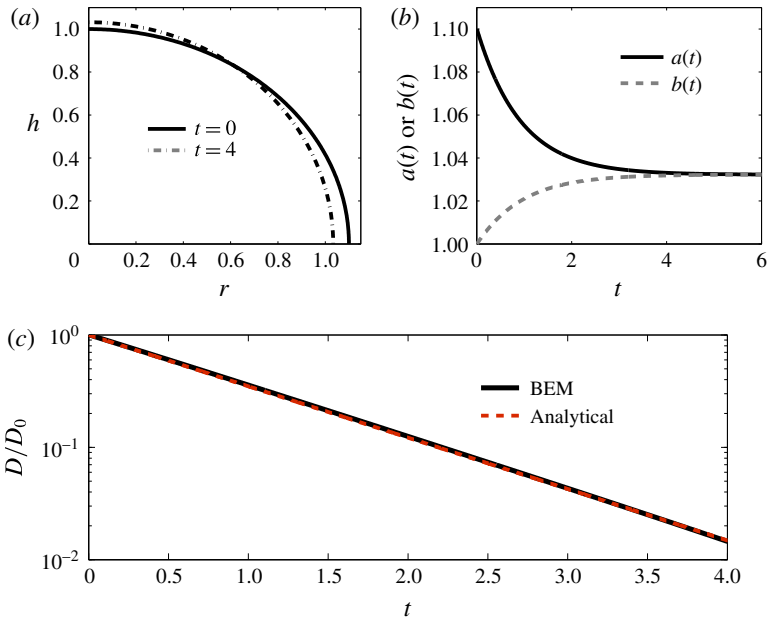

FIGURE 9. (Colour online) (*a*) The initial droplet profile and a profile close to a sphere at $t = 4$. (*b*) Time series of $a(t)$ and $b(t)$ computed by BEM. (*c*) The variable $D(t)/D_0$ computed by BEM and (A 14).

REFERENCES

BÄUMCHEN, O., FETZER, R. & JACOBS, K. 2009 Reduced interfacial entanglement density affects the boundary conditions of polymer flow. *Phys. Rev. Lett.* **103**, 247801.

BOCQUET, L. & CHARLAIX, E. 2009 Nanofluidics, from bulk to interfaces. *Chem. Soc. Rev.* **39**, 1073–1095.

BONN, D., EGGERS, J., INDEKEU, J., MEUNIER, J. & ROLLEY, E. 2009 Wetting and spreading. *Rev. Mod. Phys.* **81**, 739.

CHEN, J.-D. 1988 Experiments on a spreading drop and its contact angle on a solid. *J. Colloid Interface Sci.* **122**, 60–72.

COX, R. G. 1986 The dynamics of the spreading of liquids on a solid surface. Part 1. Viscous flow. *J. Fluid Mech.* **168**, 169–194.

CUENCA, A. & BODIGUEL, H. 2013 Submicron flow of polymer solutions: slippage reduction due to confinement. *Phys. Rev. Lett.* **110**, 108304.

EDWARDS, A. M. J., LEDESMA-AGUILAR, R., NEWTON, M. I., BROWN, C. V. & MCHALE, G. 2016 Not spreading in reverse: the dewetting of a liquid film into a single drop. *Sci. Adv.* **2** (September), 1–11.

FALK, K., SEDLMEIER, F., JOLY, L., NETZ, R. R. & BOCQUET, L. 2010 Molecular origin of fast water transport in carbon nanotube membranes: superlubricity versus curvature dependent friction. *Nano Lett.* **10** (10), 4067–4073.

FETZER, R., JACOBS, K., MÜNCH, A., WAGNER, B. & WITELSKI, T. P. 2005 New slip regimes and the shape of dewtting thin liquid films. *Phys. Rev. Lett.* **95**, 127801.

FETZER, R., MÜNCH, A., WAGNER, B., RAUSCHER, M. & JACOBS, K. 2007 Quantifying hydrodynamic slip: a comprehensive analysis of dewetting profiles. *Langmuir* **23**, 10559–10566.

DE GENNES, P. G. 1985 Wetting: statics and dynamics. *Rev. Mod. Phys.* **57**, 827.

DE GENNES, P.-G., BROCHART-WYART, F. & QUÉRÉ, D. 2003 *Capillarity and Wetting Phenomena: Drops, Bubbles, Pearls, Waves*. Springer.

https://doi.org/10.1017/jfm.2017.515 Published online by Cambridge University Press

GUIDO, S. & VILLONE, M. 1999 Measurement of interfacial tension by drop retraction analysis. *J. Colloid Interface Sci.* **209**, 247–250.

GUO, S., GAO, M., XIONG, X.-M., WANG, Y.-J., WANG, X.-P., SHENG, P. & TONG, P. 2013 Direct measurement of friction of a fluctuating contact line. *Phys. Rev. Lett.* **111**, 026101.

HAEFNER, S., BENZAQUEN, M., BÄUMCHEN, O., SALEZ, T., PETERS, R., MCGRAW, J. D., JACOBS, K., RAPHAËL, E. & DALNOKI-VERESS, K. 2015 Influence of slip on the Plateau–Rayleigh instability on a fibre. *Nat. Commun.* **6** (May), 7409.

HUH, C. & SCRIVEN, L. E. 1971 Hydrodynamic model of steady movement of a solid/liquid/fluid contact line. *J. Colloid Interface Sci.* **35**, 85–101.

LAUGA, E., BRENNER, M. P. & STONE, H. A. 2007 Microfluidics: the no-slip boundary condition. In *Springer Handbook of Experimental Fluid Mechnaics* (ed. C. Tropea, J. F. Foss & A. Yarin), pp. 1219–1240. Springer.

LEE, S. H. & LEAL, L. G. 1982 The motion of a sphere in the presence of a deformable interface. II. A numerical study of the translation of a sphere normal to an interface. *J. Colloid Interface Sci.* **87** (1), 81–106.

LEGER, L. 2003 Friction mechanisms and interfacial slip at fluid–solid interfaces. *J. Phys.: Condens. Matter* **15**, S19.

VAN LENGERICH, H. B. & STEEN, P. H. 2012 Energy dissipation and the contact-line region of a spreading bridge. *J. Fluid Mech.* **703**, 111–141.

MCGRAW, J. D., CHAN, T. S., MAURER, S., SALEZ, T., BENZAQUEN, M., RAPHAËL, E., BRINKMANN, M. & JACOBS, K. 2016 Slip-mediated dewetting of polymer microdroplets. *Proc. Natl Acad. Sci. USA* **113** (5), 1168–1173.

NETO, C., EVANS, D. R., BONACCURSO, E., BUTT, H.-J. & CRAIG, V. S. J. 2005 Boundary slip in newtonian liquids: a review of experimental studies. *Rep. Prog. Phys.* **68**, 2859.

POZRIKIDIS, C. 1992 *Boundary Integral and Singularity Methods for Linearized Flow*. Cambridge University Press.

REDON, C., BROCHARD-WYART, F. & RONDELEZ, F. 1991 Dynamics of dewetting. *Phys. Rev. Lett.* **66**, 715–718.

REITER, G. & SHARMA, A. 2001 Auto-optimization of dewetting rates by rim instabilities in slipping polymer films. *Phys. Rev. Lett.* **87** (16), 166103.

RIVETTI, M., SALEZ, T., BENZAQUEN, M., RAPHAËL, E. & BÄUMCHEN, O. 2015 Universal contact-line dynamics at the nanoscale. *Soft Matt.* **11** (48), 9247–9253.

SAHIMI, M. 1993 Flow phenomena in rocks: from continuum models to fractals, percolation, cellular automata, and simulated annealing. *Rev. Mod. Phys.* **65**, 1393.

SETU, S. A., DULLENS, R. P. A., HERNÁNDEZ-MACHADO, A., PAGONABARRAGA, I., AARTS, D. G. A. L. & LEDESMA-AGUILAR, R. 2015 Superconfinement tailors fluid flow at microscales. *Nat. Commun.* **6**, 7297.

SNOEIJER, J. H. & ANDREOTTI, B. 2013 Moving contact lines: scales, regimes, and dynamical transitions. *Annu. Rev. Fluid Mech.* **45**, 269.

SNOEIJER, J. H. & EGGERS, J. 2010 Asymptotics of the dewetting rim. *Phys. Rev.* E **82**, 056314.

SUI, Y., DING, H. & SPELT, P. D. M. 2014 Numerical simulations of flows with moving contact lines. *Annu. Rev. Fluid Mech.* **46**, 97–119.

TANNER, L. H. 1979 The spreading of silicone oil drops on horizontal surfaces. *J. Phys.* D*: Appl. Phys.* **12**, 1473–1478.

TAYLOR, G. I. 1934 The formation of emulsions in definable fields of flow. *Proc. R. Soc. Lond.* A **146**, 501.

VOINOV, O. V. 1976 Hydrodynamics of wetting. *Fluid Dyn.* **11**, 714–721; (English translation).

WEINSTEIN, S. J. & RUSCHAK, K. J. 2004 Coating flows. *Annu. Rev. Fluid Mech.* **36**, 29–53.

WINKELS, K. G., PETERS, I. R., EVANGELISTA, F., RIEPEN, M., DAERR, A., LIMAT, L. & SNOEIJER, J. H. 2011 Receding contact lines: from sliding drops to immersion lithography. *Eur. Phys. J. Special Topics* **192**, 195.

https://doi.org/10.1017/jfm.2017.515 Published online by Cambridge University Press